https://dx.doi.org/10.22161/ijaers.76.45 ISSN: 2349-6495(P) | 2456-1908(O)

Analysis of flow dynamics around two rotating circular cylinders in tandem and side by side

Alice Rosa da Silva[1], Antônio Marcos Gonçalves de Lima[2]

[1]Faculty of Civil Engineering, Federal University of Uberlândia – UFU, 38400-902 Uberlândia – MG, Brazil
[2]Faculty of Mechanical Engineering, Federal University of Uberlândia – UFU, 38400-902 Uberlândia – MG, Brazil

Abstract**—** *In this paper, the flow dynamics around two rotating circular cylinders arranged in two different configurations, in turbulent and laminar regimes are analyzed through the Immersed Boundary Methodology. The Large Eddy Simulation with dynamic Smagorinsky sub-grid scale is also used here. For the side by side and in tandem configurations, the simulations are performed, for Re 100, specific rotation 0.5 and spacing ratio varying between 1.5 and 5.0. For the first arrangement, simulations are also carried out, for Re and spacing ratio constant, and the specific rotation varying between 0 and 2. For in tandem configuration, the Re ranges from 200 to 10^5 and the others parameters are maintained constant. The results showed that the cylinder arrangements, in addition to the mentioned parameters, play an important role in the mechanism of the vortex shedding, as well as in the wake pattern and in the fluctuations of drag and lift coefficients. The rotation mechanism inhibits the vortex shedding process for different values of spacing ratio depending on the arrangement of the cylinders. Vorticity contours, time evolutions of fluid dynamics coefficients as well as pressure distribution along the cylinder are presented.*

Keywords**— Immersed Boundary Methodology, Reynolds number, rotating cylinder, spacing ratio, specific rotation.**

I. INTRODUCTION

The fluid flow with or without heat transfer is practically involved in all energy production processes, in the environmental phenomena, in the thermal equipment, in the aeronautical and aerospace engineering, in the reactor engineering, in the bioengineering and so on. In projects for automobiles and their components, in projects for rotating machines, in the sizing of anti-fire systems in large spaces, in the project of refrigeration equipment, in the forecast of pollution caused by chimneys in the atmosphere and by the discharge of pollutants into rivers, lakes and soils, in solving numerous multiphase flow problems found in the petroleum industry, etc., numerical simulation is of great importance [1].

Thus, the Computational Fluid Dynamics (CFD) has been widely used to study flows around bluff bodies, in several analyzes, as mentioned below: Silva et al. [2] investigated the flow dynamics around a pair of cylinders in different geometric arrangements for Re = 72000; Silva et al. [3] analyzed the rotation oscillation effect on the flow characteristics at low Reynolds number; Lima et al. [4] investigated vortex induced vibration in a circular cylinder mounted viscoelastically transverse to flow at moderate Reynolds; Dienstmann et al. [5] formulated a simplified model for consolidating poromechanical analyses, induced by a rigid cylinder in rotating motion immersed in a porous medium; Xia et al. [6], investigated numerically through the BGK lattice Boltzmann method, the Poiseuille flow of the fluid power law on a free rotating cylinder located eccentrically in a two-dimensional channel; Wang et al. [7], experimentally studied the flow around a circular cylinder turning retrograde near the boundary layer of a turbulent wall to Re = 10000, using the particle image velocimetry technique; Maurya et al. [8] used a rotating cylinder arranged in a rectangular T-shaped channel to investigate the heat transfer and momentum characteristics of a Bingham plastic fluid; Musmar et al. [9] investigated experimentally, the effect of rotation increment of a cylinder on the wear rate of a cylinder-piston system. The engine speed, load and the rotation angle of the cylinder were the main parameters; Zou et al. [10] investigated numerically the flow induced vibration of a rotating circular cylinder for reduced velocity in the intervals $3.0 \leq U^* \leq 14$, with the cylinder free to move in the flow direction and transverse. Bouchon et al. [11] presented a cut-cell method for the simulation of two-dimensional flows past obstacles. They showed the results of flows around an impulsively started circular cylinder for

https://dx.doi.org/10.22161/ijaers.76.45 *ISSN: 2349-6495(P) | 2456-1908(O)*

Reynolds number 1000 and 3000 and also, results of flows around a moving rigid cylinder at Re = 800. The semi-staggered grid technique was employed by Shu et al. [12] to solve several classical testing cases as flow in a channel with 180° bend, natural convection in a square cavity and lid-driven flow.

It is worth mentioning here, the Immersed Boundary Methodology (IBM), which has increasingly gained prominence in the study of flow of simple, complex, mobile and even deformable geometries, without need for rewrapping. Initially proposed by Peskin [13], it has been used and improved for different applications, such as in hydrodynamic magnet flow (MHD) with complex and mobile boundary problems [14]; in simulation of an elastic vesicle close to a wall in shear flow using the modified FI method [15]; in the mass diffusion and convection modeling through porous membranes under large deformations [16]; in problems involving heat transfer [17]; in the study of linear elliptic value problems on arbitrary domains with a Dirichlet boundary condition was proposed an augmented Immersed Boundary Method [18]; in the investigation of the flow physics behind dynamical transitions that occur in the flow field around a plunging foil [19]; among others.

In the present work, numerical simulations are performed for the analysis of two-dimensional, incompressible and isothermal flow around a pair of cylinders arranged side by side and in tandem. The influence of the spacing ratio is investigated for the two cylinders configurations, and the influence of the Reynolds number is analyzed for the aligned cylinders. Also, the rotating movement effect for the side by side case is investigated. The vorticity fields, the time evolution of the fluid dynamics coefficients, as well as the distribution of the pressure coefficient, are presented. The Immersed Boundary Methodology, together with the Virtual Physical Model is used (VPM) [20].

II. THE MATHEMATICAL MODEL

The IBM [13] together with VPM [20] are used in the present work, to simulate two-dimensional flows around two rotating circular cylinders arranged side by side and in tandem configurations. It is based on the Navier-Stokes equations plus a force term that acts so that the fluid "perceives" the interface, thus making the exchange of information between fluid and solid. In this method, the Eulerian grid represents the calculation domain and the Lagrangian grid, the immersed interface. These grids are geometrically independent and coupled through the force term.

2.1 Mathematical formulation for the fluid

The filtered Navier-Stokes equations and the continuity equation for viscous, incompressible and Newtonian flow, can be presented respectively, in tensorial form, as follow:

$$\frac{\partial u_i}{\partial t}+\frac{\partial\left(u_i u_j\right)}{\partial x_j}=-\frac{1}{\rho}\frac{\partial p}{\partial x_i}+\left[\nu_{ef}\left(\frac{\partial u_i}{\partial x_j}+\frac{\partial u_j}{\partial x_i}\right)\right]+f_i \qquad (1)$$

$$\frac{\partial u_i}{\partial x_i}=0 \qquad (2)$$

Where $\rho\ \left[Kg/m^3\right]$ and $\nu_{ef}\left[m^2/s\right]$ are respectively, the specific mass and the effective viscosity, properties that characterize the fluid. The interest variables are represented by: $u_i\ \left[m/s\right]$ is *i-th* component of the filtered velocity; $p\ \left[N/m^2\right]$ is the filtered pressure and $f_i\ \left[N/m^3\right]$ is the *i-th* component of the Eulerian force, that acts on the fluid. The source term of Eulerian force only exists in the Eulerian points coincident or close of the Lagrangian grid, being null for the other points of the domain. It is calculated by distribution of the components of the Lagrangian interfacial force vector $\vec{F}\left(\vec{x}_k\right)\ \left[N\right]$, using a distribution function, as proposed by Peskin and McQueen [21]. The equation for Lagrangian force can be expressed as:

$$\vec{F}\left(\vec{x}_k,t\right)=\underbrace{\rho\frac{\partial\vec{V}\left(\vec{x}_k,t\right)}{\partial t}}_{\vec{F}_a}+\underbrace{\rho\vec{\nabla}.\left(\vec{V}\left(\vec{x}_k,t\right)\vec{V}\left(\vec{x}_k,t\right)\right)}_{\vec{F}_i}-\underbrace{\vec{\nabla}.\left[\mu\left(\vec{\nabla}\vec{V}\left(\vec{x}_k,t\right)+\vec{\nabla}^T\vec{V}\left(\vec{x}_k,t\right)\right)\right]}_{\vec{F}_v}+\underbrace{\vec{\nabla}p\left(\vec{x}_k,t\right)}_{\vec{F}_p} \qquad (3)$$

In (3) $\vec{F}_a\ \left[N\right]$ is the acceleration force, $\vec{F}_i\ \left[N\right]$ is the inertial force, $\vec{F}_v\ \left[N\right]$ is the viscous force and $\vec{F}_p\ \left[N\right]$ is the pressure force.

2.2 Indicator function

The indicator function, proposed by Unverdi and Trygvason [22] is also used in the present work. It is an interface tracking method, where the function is calculated in whole domain or in part of it, with the attribution of the unit value for internal points to the interface, zero for the external points and values between zero and unit for the transition points, that is, on the interface. This function is based on a function $\vec{G}\left(\vec{x},t\right)$ and can be expressed by:

$$\vec{\nabla}I\left(\vec{x},t\right)=\vec{G}\left(\vec{x},t\right) \qquad (4)$$

The term on the right side of (4) is given by:

https://dx.doi.org/10.22161/ijaers.76.45 *ISSN: 2349-6495(P) | 2456-1908(O)*

$$\vec{G}(\vec{x},t)=\sum_k D_{ij}(\vec{x}-\vec{x}_k)\vec{n}(\vec{x}_k)\Delta S(\vec{x}_k) \quad (5)$$

In (5) $\vec{n}(\vec{x}_k)$ is the normal vector of the interface.

Applying the divergent operator in (4), the Laplacian of the indicator function is obtained:

$$\vec{\nabla}^2 I(\vec{x},t)=\vec{\nabla}\vec{G}(\vec{x},t) \quad (6)$$

In this way, after solving (6), the solution of the indicator function is obtained, $I(\vec{x},t)$, in all points of the domain. For the resolution of the linear system resulting from the discretization of (6), the SIP solver is used.

2.3 Turbulence model

Turbulence is one of the most challenging problems of the modern physical and it is among the most complex and fascinating phenomena found in the nature. Due to several practical implications in different sectors, the number of researches related to the understanding and control of turbulent flows has become increasingly greater. An alternative for the treatment of flows at high Reynolds number can be done by scales separation. This separation can be accomplished through the decomposition process of the Navier-Stokes equations into a mean and a floating part, as proposed by Reynolds [23], or through a filtering process proposed by Smagorinsky [24]. Here, the Large Eddy Simulation (LES) is used, for which the filtering process is necessary. For the turbulent viscosity calculation, used in LES, there are different sub-grid models. In the present work, the sub-grid model of Smagorinsky is used, which is based on the hypothesis that the production of the sub-grid turbulent tensions is equal to the dissipation. The turbulent viscosity is given as a function of the strain rate and the length scale. The Smagorinsky constant used here is 0.18 for isotropic and homogeneous turbulence.

III. NUMERICAL METHOD

For the velocity-pressure coupling, the Fractional Step Method is used, initially proposed by Chorin [25]. It is a non-iterative method, where from the fields of u, υ, p and f of the previous iteration, the velocity fields are estimated. With these estimated fields, the pressure correction is calculated, through the solution of the linear system, by the Modified Strongly Implicit Procedure (MSI) developed by Scheneider and Zedan [26]. The pressure behaves like a Lagrange multiplier in minimization problems. The importance of the Poisson equation for the pressure correction is that it makes the connection between the momentum equations and continuity. It provides values of p that allow that the values of the velocity components u^{n+1} and υ^{n+1}, obtained from the respective Navier-Stokes equations, satisfy the mass conservation in the instant of time $n+1$. Thus, the estimates of the velocity components, $\tilde{u}^{n+1}$, obtained with information from the fields u, υ, p and f of the preceding time, are:

$$\frac{\tilde{u}_i^{n+1}-u_i^n}{\Delta t}+\left[\frac{\partial(u_i u_j)}{\partial x_j}\right]^n=-\frac{1}{\rho}\frac{\partial p^n}{\partial x_i}+\frac{\partial}{\partial x_j}\left[\nu_{ef}\left(\frac{\partial u_i}{\partial x_j}+\frac{\partial u_j}{\partial x_i}\right)\right]^n+f_i^n \quad (7)$$

Making the appropriate arrangements, obtain:

$$\frac{\tilde{u}_i^{n+1}-u_i^{n+1}}{\Delta t}=\frac{1}{\rho}\frac{\partial(p^{n+1}-p^n)}{\partial x_i} \quad (8)$$

After the application of the divergent operator $\frac{\partial}{\partial x_i}$ on both sides of (8), follows:

$$\frac{1}{\Delta t}\left[\frac{\partial \tilde{u}_i^{n+1}}{\partial x_i}-\frac{\partial u_i^{n+1}}{\partial x_i}\right]=\frac{1}{\rho}\frac{\partial}{\partial x_i}\left(\frac{\partial p'^{n+1}}{\partial x_i}\right) \quad (9)$$

On what $p'^{n+1}=p^{n+1}-p^n$ is the correction pressure. The importance of the divergent is due to the fact that it is one of the terms in the equation that expresses the mass conservation. As it is necessary that the velocity field satisfy the continuity equation, the second term on the left side of (9), $\frac{\partial u_i^{n+1}}{\partial x_i}$, will be null. Therefore, the equation can be rewritten as:

$$\frac{1}{\Delta t}\frac{\partial \tilde{u}_i^{n+1}}{\partial x_i}=\frac{1}{\rho}\frac{\partial^2 p'^{n+1}}{\partial x_j \partial x_j} \quad (10)$$

Rearranging (10), a Poisson equation for the pressure correction is obtained, whose source term is the divergent of the estimated velocity:

$$\frac{\partial^2 p'^{n+1}}{\partial x_j \partial x_j}=\frac{\rho}{\Delta t}\frac{\partial \tilde{u}_i^{n+1}}{\partial x_i} \text{ or } \nabla^2 p'^{n+1}=\frac{\rho}{\Delta t}\vec{\nabla}.\vec{\tilde{u}}^{n+1} \quad (11)$$

Thus, the estimated velocity fields are obtained through (7) and the pressure correction field, through the resolution of the linear system, generated by discretization of (11). From (8), the velocity field is updated by solving (12):

$$u_i^{n+1}=\tilde{u}_i^{n+1}-\frac{\Delta t}{\rho}\frac{\partial p'^{n+1}}{\partial x_i} \quad (12)$$

For the time advance of the momentum equations, second order Adams-Bashforth is used and, for the first iteration,

https://dx.doi.org/10.22161/ijaers.76.45 *ISSN: 2349-6495(P) | 2456-1908(O)*

the first order Euler method. Thus, the discretization of the components x and y of the estimated velocity is given respectively by:

$$\tilde{u}_{i,j}^{n+1} = u_{i,j}^{n} + \Delta t\left[1{,}5\left(-A_{xi,j}^{n} + D_{xi,j}^{n}\right) - 0{,}5\left(-A_{xi,j}^{n-1} + D_{xi,j}^{n-1}\right)\right] - \\ -\Delta t\left(\frac{1}{\rho}P_{xi,j}^{n} + f_{xi,j}^{n}\right) \quad (13)$$

$$\tilde{\upsilon}_{i,j}^{n+1} = \upsilon_{i,j}^{n} + \Delta t\left[1{,}5\left(-A_{yi,j}^{n} + D_{yi,j}^{n}\right) - 0{,}5\left(-A_{yi,j}^{n-1} + D_{yi,j}^{n-1}\right)\right] - \\ -\Delta t\left(\frac{1}{\rho}P_{yi,j}^{n} + f_{yi,j}^{n}\right) \quad (14)$$

For the Navier-Stokes equations, the second-order centered finite differences in space are used. A displaced arrangement is adopted for the velocity components because it provides more stability in the pressure-velocity coupling. For the discretization of the Lagrangian force, the calculation of the existing derivatives, is done through the Lagrange polynomials using auxiliary points in the x and y directions. Thus, to determine the variables in the auxiliary points and in the points of the Lagrangian mesh, interpolations are made from the Eulerian mesh variables.

IV. PROBLEM DESCRIPTION

The simulations are carried out in a non-uniform mesh of 600x300 points, calculation domain 50Dx30D, being D the cylinder diameter. Downstream from the cylinder center until the end of the domain is higher than 26D. According to Prasanth et al. [27], the boundary downstream of the cylinder, at a distance equal to or greater than 25.5D, has no significant effect on the flow and in the cylinder response. On the other hand, Chen and Zha [28], after intensive numerical experiments, concluded that the solution is not influenced when the downstream boundary is located 20D from the cylinder center.

For the two circular cylinders arranged side by side, θ = 90º, the upper cylinder rotates in the clockwise direction and the lower cylinder in the counterclockwise direction, Fig. (1a). For in tandem cylinders case, θ = 180°, the upstream cylinder rotates in the clockwise direction whereas the downstream cylinder in the counterclockwise direction, Fig. (1b).

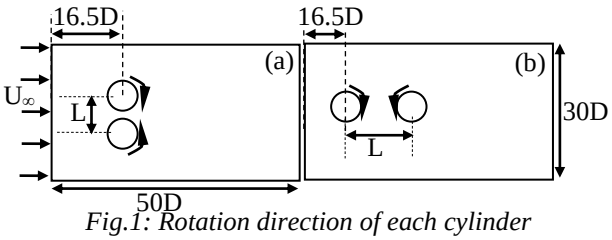

Fig.1: Rotation direction of each cylinder

The movement is imposed around its own axis through the imposition of the velocity components at each Lagrangian point. For this, the tangential velocity is decomposed.

V. RESULTS AND DISCUSSION

The study of the flow around one or more stationary cylinders obtained by several authors, is of great importance to contribute to a better understanding of the flow dynamics when cylinders are in motion. In this section, are presented the results of the numerical simulations, carried out considering two rotating circular cylinders side by side and in tandem, in order to investigate the spacing ratio, the specific rotation and the Reynolds number effect on the flow characteristics.

5.1 Influence of the spacing ratio on the flow around a pair of cylinders side by side

Here, the vorticity fields are presented as well as the time evolution of the fluid dynamics coefficients and the respective mean values, for laminar flow regime.

5.1.1 Vorticity fields

Figure 2 shows the vorticity fields for Re = 100, α = 0.5, spacing ratios 1.2, 1.5, 2.0, 2.5, 3.0, 3.5, 4.0 and 5.0 and, the Fig. (2g) shows the vorticity contour, obtained by Yoon et al. [29].

For the spacing ratio 1.2, Fig. (2a), the two cylinders behave as one, due to the great proximity between them and the rotation movement in opposed directions. In this way, shear layers move from the upper and lower cylinders and merge to form a single wake downstream. With the increase of the spacing ratio, Fig. (2b), the flow behaves very different from the one observed in Fig. (2a). Downstream, positive and negative vorticity can be observed at the bottom and at the top sides, respectively from both cylinders; however, the vortices are not detached close to the cylinder, remaining as a single elongated vortex. It is even reasonable to say that for L/D = 1.5, the rotation movement of the two cylinders inhibited the vortex shedding process, even with a rotation equal to 0.5, which is confirmed in Fig. (3a). In the results presented by Xiao-hui et al. [30], for Re = 450 and T/D = 1.11, the

https://dx.doi.org/10.22161/ijaers.76.45 *ISSN: 2349-6495(P) | 2456-1908(O)*

suppression of vortex shedding was obtained for rotation equal to 1.74. In Fig. (2c), the shear layers on both sides of each cylinder are visible, however, one cylinder influences the other so that the vortex shedding process until is not yet completely independent. For this spacing ratio, the flip-flopping pattern is observed. It is also verified by Yoon et al. [29], for stationary cylinders and g* = 0.7, Fig. (2g). For L/D = 2.5 the shear layers from both cylinders cause in phase synchronized vortex shedding in the first dimensionless times, approximately 50 and after the vortex shedding is out of phase, as shown in Fig. (3j). It is also noted that the opposite rotational movements contribute to the formation of a single wake more or less elliptical downstream of the cylinders. It is worth mentioning that, far from the two cylinders, the wake is narrower than close to them. This behavior is reported in Zdravkovich [31], for side by side stationary cylinders and 1.1-1.2 < T/D < 2-2.2. The same does not happen for L/D = 3.0, in which just downstream, alternating vortices, in phase, are detached from each cylinder, in the first dimensionless times, approximately ≤ 200. During this interval of time, the vortex shedding process is regular and the wake formed downstream of two cylinders is clearly independent. After, the vortex shedding process, goes through a transition so that two independent wakes no more exist giving way to a wake with shape more or less elliptical. The vortices are also released out of phase and, along of the wake, several vortices pairs of lesser intensity are noted. For L/D ≥ 3.5, a symmetrical pattern of anti-phase flow is observed. This characteristic is also seen for the case of two stationary cylinders side by side, for T/D = 4.0 [32]. However, as the cylinders have opposite rotation movement, although it is verified through the vorticity fields, the fluctuations produced by the vortex shedding process are in phase, as shown by the time evolution of the drag coefficients for L/D ≥ 3.5. Here, for these spacing ratios, two vortices wakes are also independent as described by many authors, for the stationary case. It is also pointed out, that the opposite movement of the two cylinders leads to symmetrical wakes in relation to the central line of the flow. It can be concluded from Fig. 2, that the spacing ratio as well as the rotation movement, have an important effect on the vortex shedding pattern, in the separation of the shear layers and consequently on the wake pattern.

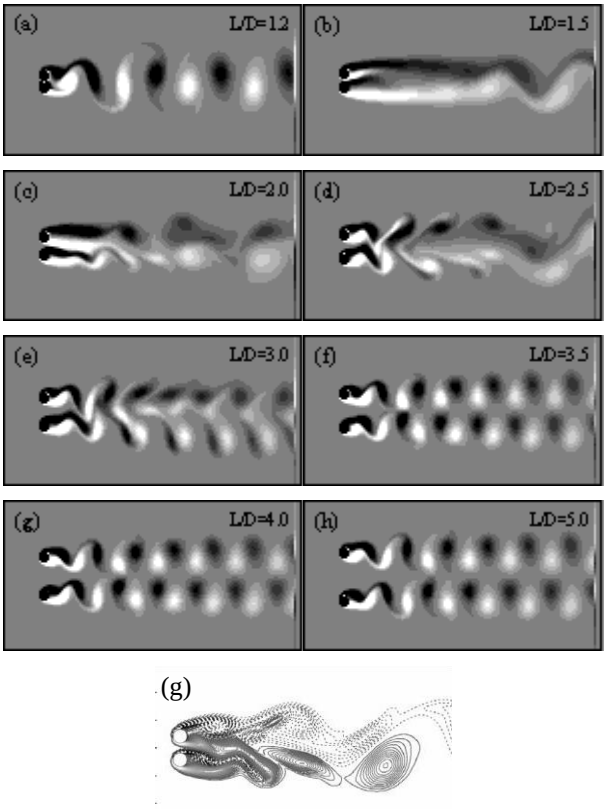

Fig.2: Vorticity fields for Re = 100, α = 0.5 and 1.2 ≤ L/D ≤ 5.0. (g) extracted from Yoon et al. [29], for α = 0.0 and g = 0.7*

5.1.2. Time evolution of the fluid dynamics coefficients

Figure 3 shows the time evolution of the drag coefficient, for the same data as in Fig. 2. The left column corresponds to the lower cylinder and the right column to the upper cylinder. It is observed that the fluctuations show similar behavior for the two cylinders, for all spacing ratios.

For L/D = 1.2, the fluctuations are periodic and no sinusoidal. It is worth mentioning that, although the amplitudes of these, for the both cylinders have the same tendency, the fluctuations are out of phase. For L/D = 1.5, the fluctuations amplitude decreased drastically, keeping it approximately uniform throughout the simulation. This confirms the great influence of the rotation in the vortex shedding process, for this spacing ratio, as shown in Fig. (2b). For L/D = 2.0, the fluctuations show an irregular behavior over the time, corresponding to the flip-flopping pattern. For the spacing ratio equal to 2.5, the fluctuations are synchronized in phase for the dimensionless time approximately up to 50, as already commented. After, "kinks" appear in the fluctuations, which are similar for both cylinders, just lagged in time, Fig. (3j). This behavior is due to the shape more or less elliptical of the wake, far

https://dx.doi.org/10.22161/ijaers.76.45 *ISSN: 2349-6495(P) | 2456-1908(O)*

from the cylinders, Fig. (2d), and due to vortex fusion, that occurs during the vortex shedding process. For L/D = 3.0 the fluctuations for the drag coefficient are periodic, sinusoidal and of great amplitudes for the dimensionless time ≤ 200. After these times, the fluctuations remain regular, but with less amplitude. This behavior is due to the change in the wake pattern, throughout the simulation, as previously commented. For the spacing ratios ≥ 3.5, the drag fluctuations present similar behavior for both cylinders, with slight reduction in amplitude as the spacing is increased. It is interesting to point out that although the vorticity fields show an anti-phase flow pattern, Fig. 2, as classified for the case of two side by side stationary cylinders, here, as the cylinders are in opposite rotation movement, the drag fluctuations for the two cylinders are synchronized in phase, as already commented. For a better understanding of what is being exposed, a zoom has been done, considering L/D = 4.0 for the fluctuations of the both cylinders, Fig. (3i).

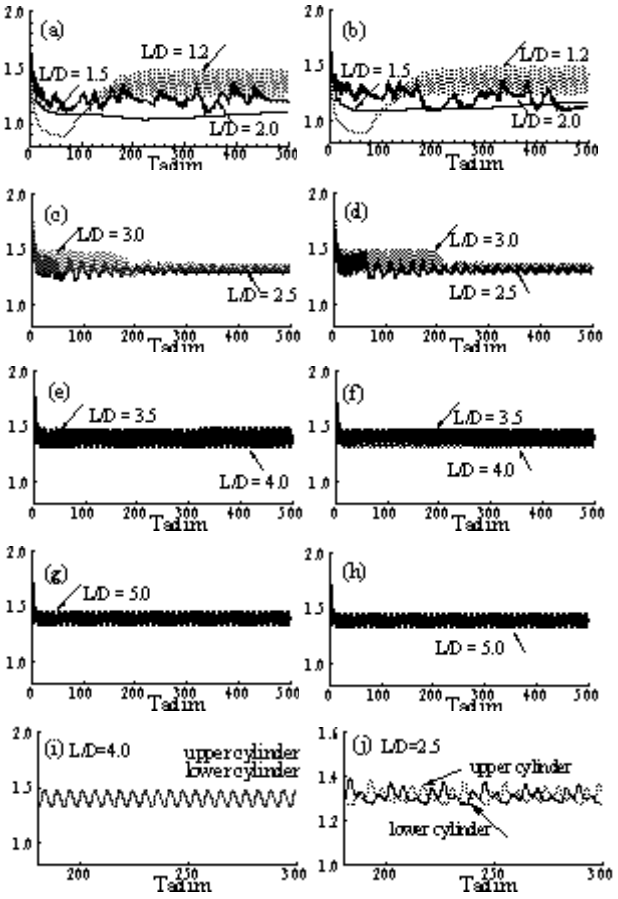

Fig. 3: Time evolution of the drag coefficients, for Re = 100, α = 0.5 and several spacing ratios.

Figure 4 shows the time evolution of the lift coefficient, for the same data of the Figs. 2 and 3. The left column corresponds to the lower cylinder and the right column to the upper cylinder. The behavior presented for all spacing ratios is also similar for both cylinders. It is interesting to point out that the vortex shedding process and the wake pattern have different effects on drag and lift coefficients. For spacing ratio equal to 2.5, the lift fluctuations are in phase, as shown in Fig. (4i), contrary of drag fluctuations that are lagged in time, Fig. (3j). For L/D ≥ 3.5, again opposite to what is observed for the drag fluctuations, the lift fluctuations are anti-phase, as can be seen by zoom made for L/D = 4.0, Fig. (4j). It is worth mentioning that for all spacing ratios, the lift obtained for the lower cylinder (counterclockwise rotation) is negative and the obtained for the upper cylinder (clockwise rotation) is positive. This behavior is expected once a time that, the velocity at the top of the upper cylinder (same direction of the flow) is greater than the bottom (opposite direction of the freestream velocity).

As a result, the pressure at the bottom is greater, causing a positive lift force. On the other hand, for the lower cylinder, the velocity at the top is in the opposite direction of the flow, being, therefore, smaller than that the bottom (same direction of the freestream velocity). Consequently, the higher pressure at the top, causes a negative lift coefficient.

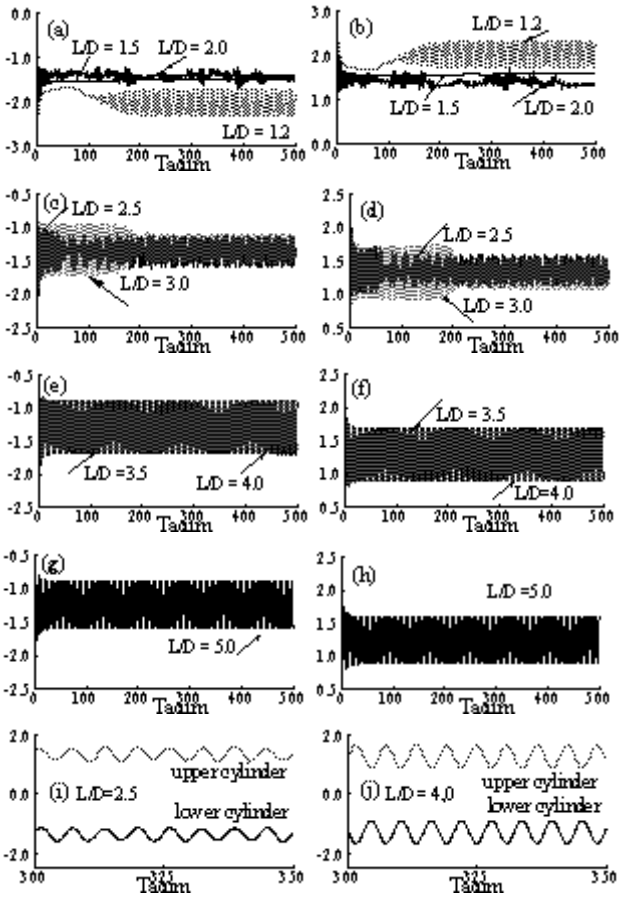

Fig. 4: Time evolution of the lift coefficients, for Re = 100, α = 0.5 and several spacing ratios.

https://dx.doi.org/10.22161/ijaers.76.45 *ISSN: 2349-6495(P) | 2456-1908(O)*

Figure 5 shows for better understanding, the mean values of the fluid dynamics coefficients for the two cylinders, placed side by side. With the exception of what is observed for L/D = 1.5, the mean values of the drag coefficients for both cylinders, are practically the same. On the other hand, the mean values of the lift coefficients have opposite behaviors, due to the direction of the cylinder rotation. Here, the positive lift generated by the upper cylinder with clockwise rotation, and, the negative lift generated by the lower cylinder with counterclockwise rotation, are better visualized.

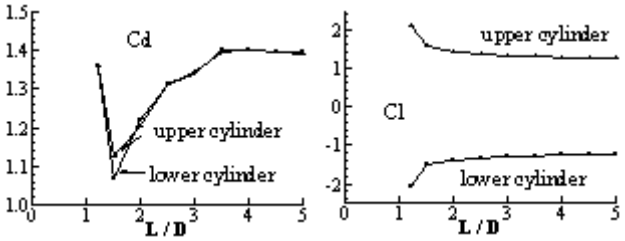

Fig. 5: Mean values of the drag and the lift coefficients as a function of the L/D for side by side cylinders.

5.2 Influence of the specific rotation on the flow around a pair of cylinders side by side

In this section the vorticity fields as well as the mean values of the drag and lift coefficients are presented, for Re = 100, L/D = 1.2 and $0 \leq \alpha \leq 2.0$.

5.2.1 Vorticity fields

The flow visualization by the vorticity contours is shown in Fig. 6, after the flow has reached the permanent regime. It can be noted the negative vorticity generated by the upper cylinder and the positive vorticity generated by the lower cylinder, as a single body. One probable reason for this behavior is that the cylinders are rotating in opposite direction from each other. The interaction between two shear layers originated from each cylinder occurs only at downstream of the cylinders, as expected. There is a '2S' mode of vortex shedding in the classical Von Kármán Street. Then, the wake formed behind them is symmetrical in relation to the center of the domain. As can be seen, the results show that the cylinder rotation has an important effect on the vortex shedding process. This mechanism is suppressed as the specific rotation increases. In this way, the flow reaches a steady state, without vortices, at the critical specific rotation equal to 1.3.

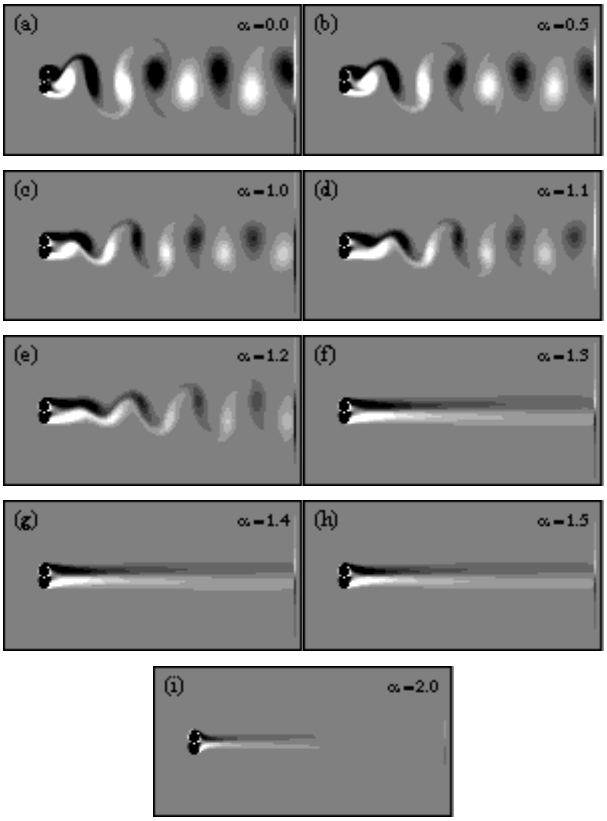

Fig. 6: Vorticity contours for Re = 100, L/D = 1.2 and $0 \leq \alpha \leq 2.0$.

The mean values of the fluid dynamics coefficients of the present study are compared with the numerical results of Yoon et al. [29]. Fig. (7a) shows the mean values of the lift coefficients for the upper and lower cylinders, and Fig. (7b) the mean values of the drag coefficients. The lift coefficients are equals for both cylinders, however with opposite values. The lower cylinder has negative mean values while the upper cylinder presents positive mean values, for all analyzed specific rotation.

It can be observed, Fig. (7a), that the mean values decrease with an increase of the specific rotation for the lower cylinder, presenting a little increase for $\alpha = 2.0$. On the other hand, the values increase as the specific rotation is increased for the upper cylinder. In Fig. (7b) it is noted that the mean values of the drag coefficients decrease with an increase of the specific rotation. This is coherent once a time that, the vortex shedding mechanism is suppressed as the specific rotation increases, as shown in Fig. 6. The obtained results presented good agreement with the numerical results of Yoon et al. [29].

https://dx.doi.org/10.22161/ijaers.76.45 *ISSN: 2349-6495(P) | 2456-1908(O)*

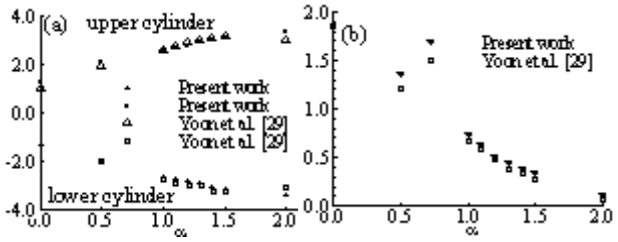

Fig. 7: Mean values: lift coefficients a) and drag coefficients b)

5.3 Influence of the spacing ratio on the flow around a pair of cylinders placed in tandem

Here, the vorticity fields are presented, as well as the time evolution of the fluid dynamics coefficients and the respective mean values, for laminar flow regime Re = 100, α = 0.5 and spacing ratios equals to 1.5, 2.0, 2.5, 3.0, 3.5, 4.0, 4.5 and 5.0.

5.3.1 Vorticity fields

The flow visualization by vorticity contours is shown in Fig. 8 after the flow has reached the permanent regime. Here, the upstream one has a clockwise rotation movement and the downstream one has a counterclockwise rotation. For spacing ratio from 1.5 to 3.5, Figs. (8a) to (8e), the both cylinders behave as a single bluff body and the vortex shedding process reduces as the spacing ratio increases. It is also noted that the vortices behind the cylinders are more elongated, which reduces the drag on the upstream cylinder as the spacing increases. On the other hand, as the downstream cylinder is surrounded by the shear layers of the upstream cylinder, consequently in a region of lower pressure, the drag on it is significantly less than that of the upstream cylinder. It interesting to point out that, for L/D equals to 3.0 and 3.5, the vortex shedding process occurs normally for the first times of simulation and decreases as time advances. For spacing ratios from 4.0 to 5.0, the vortex shedding process of the upstream cylinder becomes more independent, as well as that of the downstream cylinder. It is also verified that the generated vortices are closer to each other, are more robust and have a rounded shape, differently from what is observed for smaller spacing (vortices more elongated). As a result, the drag on two cylinders increased. From the presented results, it is clearly confirmed that the influence of the spacing ratio as well as the rotation movement in the suppression of the vortex shedding mechanism, depends on the cylinders arrangement.

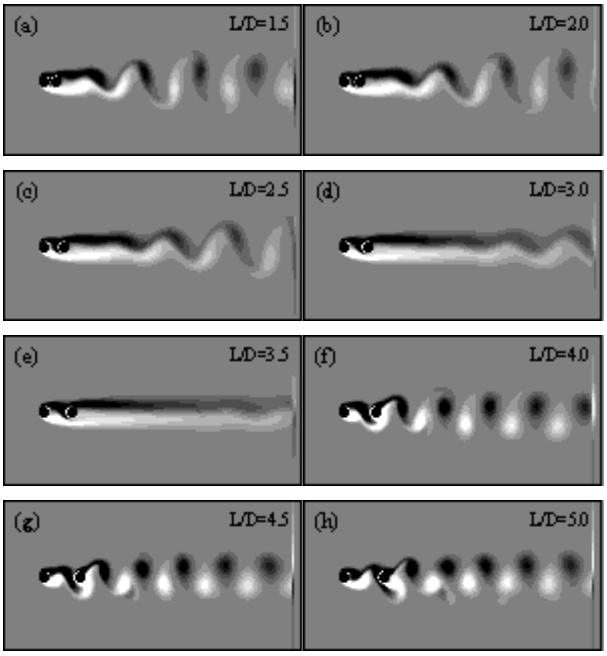

Fig. 8: Vorticity contours for Re = 100, α = 0.5 and 1.5 ≤ L/D ≤ 5.0.

5.3.2 Time evolution of the fluid dynamics coefficients

Figure 9 shows the time evolution of the drag coefficients, for cylinders in tandem, Re = 100, α = 0.5 and 1.5 ≤ L/D ≤ 5.0. As previously mentioned, the vortex shedding process is influenced by the spacing ratio and the rotation movement of the cylinders. Consequently, it also reflects in the amplitude of the fluctuations of the drag coefficients for both cylinders, which reduces as the spacing ratio increases up to 3.5, even keeping the constant rotation. Thus, for L/D = 3.0 and 3.5, the vortex shedding process occurs only in the first times of simulation. As time progresses, even for these spacing, due to the influence of the rotation movement, the vortex shedding process has been suppressed, consequently, the drag fluctuations as well. For L/D ≥ 4.0, the amplitude of the fluctuations increases significantly, compared to those observed for small spacing ratios. This is consistent, once a time that the generated vortices are stronger and more rounded, Figs. (8f) to (8h). It is also noted that the fluctuations amplitude remained practically the same with the increase of the spacing ratio, for both cylinders.

https://dx.doi.org/10.22161/ijaers.76.45 *ISSN: 2349-6495(P) | 2456-1908(O)*

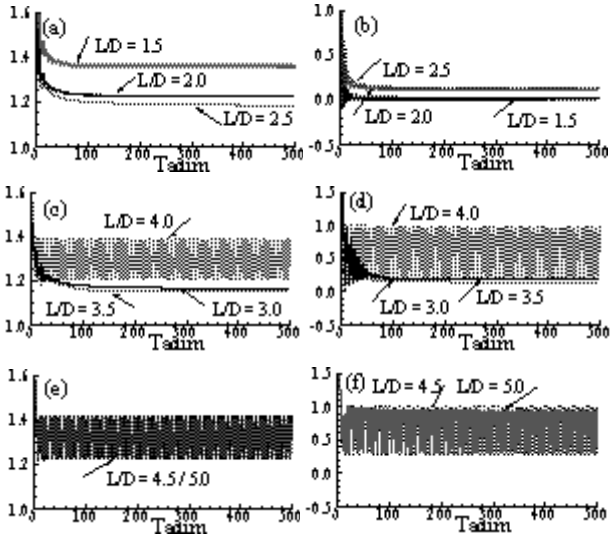

Fig. 9: Time evolution of the drag coefficients, for upstream cylinder (left column) and downstream cylinder (right column).

Figure 10 shows the time evolution of the lift coefficient for the same spacing ratios as in Fig. 9. For L/D = 3.0 and 3.5, fluctuations for the dimensionless time greater than 100 are no longer observed. On the other hand, for 3.5 < L/D < 3.0 the rotation movement had no effect in suppressing the vortex shedding process. It is noted that, for the upstream cylinder, the fluctuations amplitude decreases as the spacing ratio increases up to 3.5 and increases with further increase in L/D. This behavior is coherent once a time that, for L/D > 3.5, the vortex shedding mechanism occurs normally. The same behavior is verified for the downstream cylinder. However, the amplitude of the fluctuations is greater.

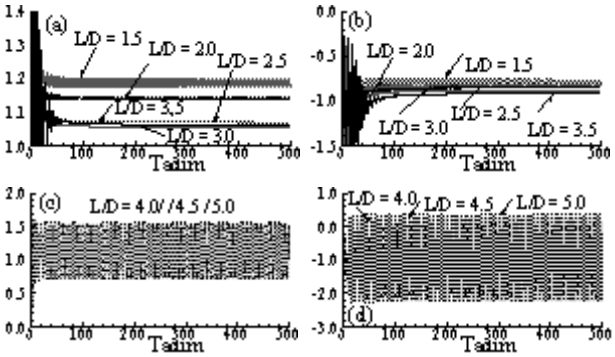

Fig. 10: Time evolution of the lift coefficients, for upstream cylinder (left column) and downstream cylinder (right column).

It is worth mentioning that, the upstream cylinder has a positive lift coefficient, once a time that, has a clockwise rotation movement, whereas the downstream cylinder has a negative lift coefficient, due to the counterclockwise direction movement.

Figure 11 shows the mean values of the drag and lift coefficients for the upstream and downstream cylinders, aiming at a better understanding of the previous Figs., (9) and (10). It can be seen that the drag exerted on both cylinders has opposite effects for L/D up to 3.5, this is, for the upstream cylinder, the drag reduces as the spacing increases and for the downstream cylinder, the drag increases. With further increase in the L/D, there is an increase in the mean value of the drag for both cylinders, being more significant in the downstream one. The explanation for this behavior is well visualized in Fig. 8, in which, for L/D = 3.5, the vortex shedding process is practically suppressed, due to the rotation movement, while for L/D > 3.5, the wake vortices is visualized. The mean values of the lift coefficient gradually reduce with increasing spacing ratio up to 4.0 for the downstream cylinder and then gradually increase as well. For the upstream cylinder, this increase is observed from a smaller spacing ratio (L/D = 3.0), after which the mean value grows and remains practically constant after L/D = 4.0.

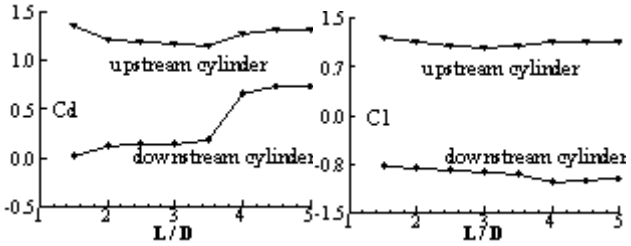

Fig. 11: Mean values of the drag and lift coefficients in function of L/D

It is interesting to note, that the rotation movement of the cylinders, produces more significant changes in the drag than in the lift, as shown in Fig. 11.

5.4 Influence of the Reynolds number for in tandem cylinders

Figure 12 shows the time histories of the drag coefficient for the upstream cylinder, considering the laminar and turbulent flow regime, L/D = 2.0, α = 0.5. It is clearly noted that the drag on the cylinder decreases continuously as the Re increases, Fig. (12a). For Re ≤ 500, the fluctuations are periodic, which corresponds to the alternating vortex shedding process, with the formation of the classical Von Kármán Street downstream of the two cylinders.

https://dx.doi.org/10.22161/ijaers.76.45 *ISSN: 2349-6495(P) | 2456-1908(O)*

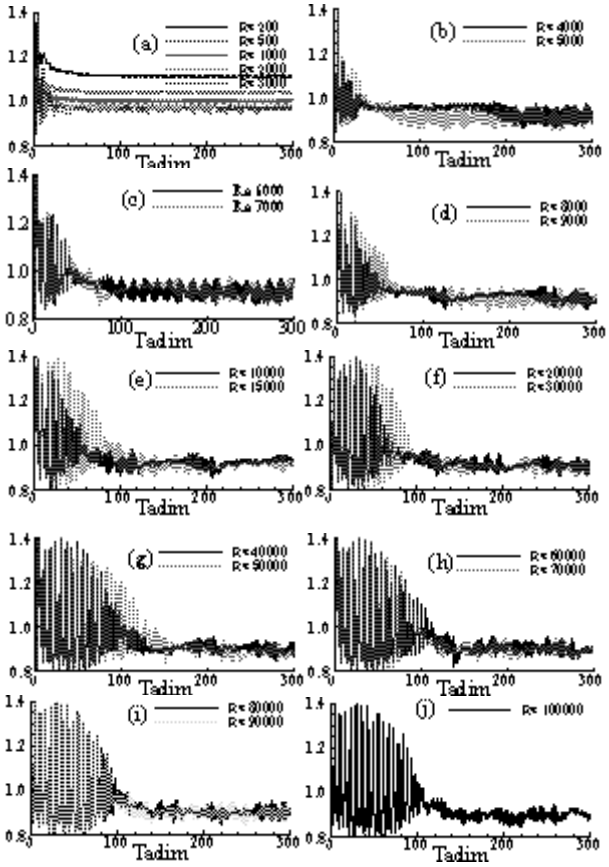

Fig. 12: Time evolution of the drag coefficients, for upstream cylinder, $200 \leq Re \leq 10^5$.

For Re 1000 and 2000, the fluctuations pattern is similar. It is noted the presence of "kinks" in the fluctuations along the time evolution, indicating the generation of more than one vortex per cycle. The wake seems disorganized, with vortices pairs scattered along it and, with different size and strength. The "kinks" pattern changes for Re = 3000, indicating a greater number of weak and strong vortices per cycle. It is interesting to note that for Re = 4000, there is a reduction in the mean value of the drag coefficient throughout the simulations. For the dimensionless time approximately between 40 and 173, the mean value is 0.9585, while for the rest of the time it is 0.9248. In addition, there is a reduction in the amplitude of the fluctuations for the mentioned time intervals. As increases the Re, the increase in the amplitude in the first dimensionless time became more considerable, being accompanied by a sharp reduction. In addition, the presence of envelopes, in a greater or lesser amount, for the cases with Re ≥ 5000, is observed.

It can be seen from obtained results, that although the numerical simulations are two dimensional, with the increase in the Re and the preponderance of the inertial forces over the viscous forces, three-dimensional instabilities develop, turbulence levels begin to appear, which influences the vortex shedding process, even though the periodicity still remains robust [33]. Such instabilities, as well as the totally disorganized vortex street certainly reflect in the drag and changes the fluctuations pattern as shown in Fig. 12.

Figure 13 shows the time evolution of the drag coefficient for the downstream cylinder. The shear layers at the top of the upstream cylinder, in a clockwise rotation movement, collide with the downstream cylinder, while

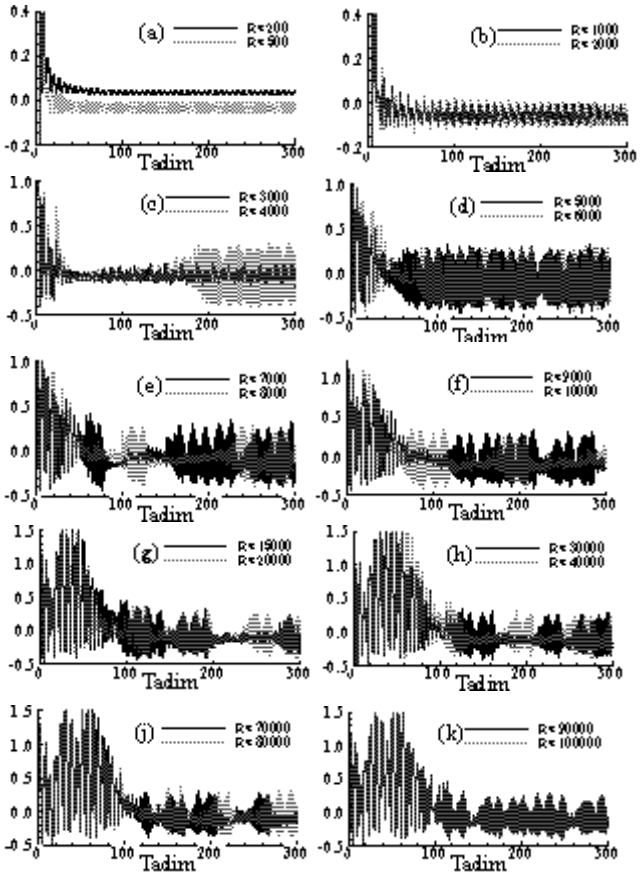

Fig. 13: Time evolution of the drag coefficients, for downstream cylinder, $200 \leq Re \leq 10^5$.

those originating from the bottom, surround the downstream cylinder, causing smaller drag and greater fluctuations amplitude.

For the two first simulated Re, the fluctuations pattern is similar to that observed for the upstream cylinder. In addition, it is clearly noted, that the mean drag is positive for Re = 200. With the increase of Re up to 3000, the fluctuations pattern is no longer sinusoidal and differs from that observed for the upstream cylinder. And, it is noted that the mean drag has a negative value. For Re = 4000, two different fluctuations pattern are verified, which implies that the vortex shedding pattern has changed over

https://dx.doi.org/10.22161/ijaers.76.45 *ISSN: 2349-6495(P) | 2456-1908(O)*

the simulations. With further increase in the Reynolds number, there is a considerable increase in the amplitude of the fluctuations, for the first dimensionless time and after, a sharp reduction. This behavior is also observed for the upstream cylinder.

Figure 14 shows the time histories of the lift coefficient for the upstream cylinder. Note that the lift coefficient is positive for all analyzed Reynolds number. This is coherent, once a time that, as the upstream cylinder rotates in the clockwise direction, the velocity at the top of the cylinder is greater than at the bottom.

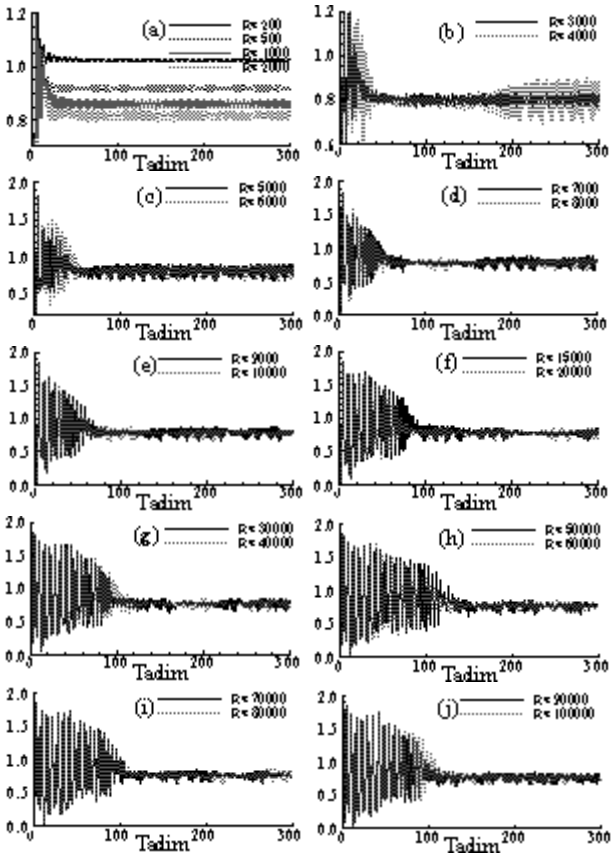

Fig.14: Time evolution of the lift coefficient for the upstream cylinder, $200 \leq Re \leq 10^5$.

As a result, the pressure at the bottom is greater, causing a positive lift force. It is also worth to note, that the coefficient reduces as the Re increases, with a slight increase from Re 6000 to 8000 and then remains approximately constant for the others Re, with small variations. It is clearly observed that the fluctuations pattern varies along of the simulations, which implies that the vortex shedding process has been changed.

The time evolution of the lift coefficient for the downstream cylinder is shown in Fig. 15. Contrary to what is observed for the upstream cylinder, Fig. 14, the downstream cylinder has a negative lift coefficient for all analyzed Re. This is due to the fact that, with the counterclockwise rotation movement, the velocity at the top of the cylinder is smaller than that of the bottom and, consequently, the pressure at the top is greater, resulting in a negative lift coefficient. It is also observed that the fluctuations amplitude for the downstream cylinder are greater than for the upstream one, with a behavior approximately similar to that observed in Fig. 14.

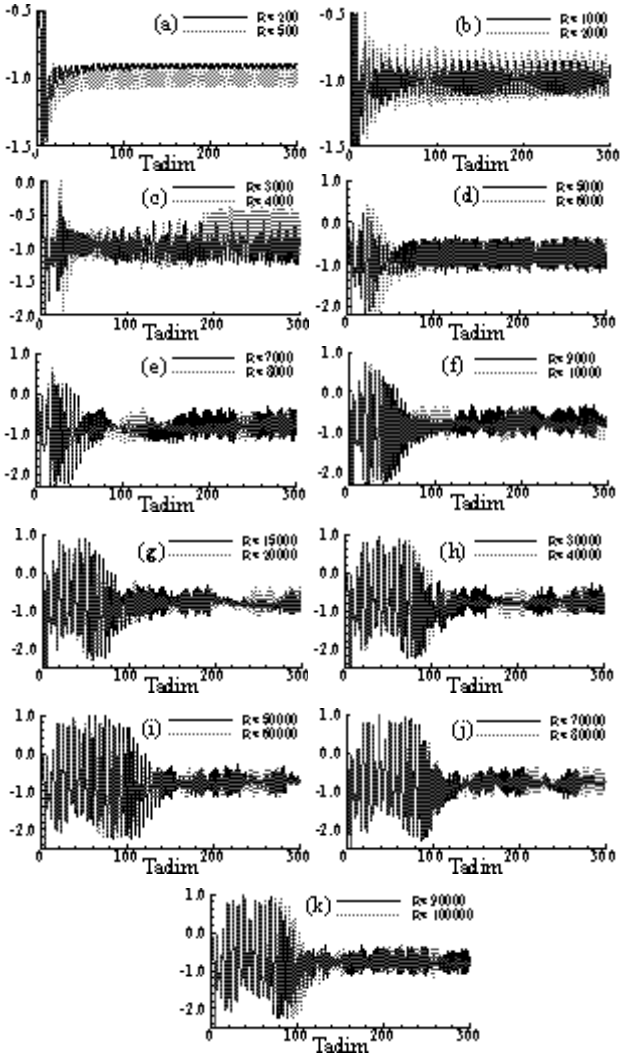

Fig. 15: Time evolution of the lift coefficient for the downstream cylinder, $200 \leq Re \leq 10^5$.

5.5 Influence of the Reynolds number in the pressure coefficient

The influence of the Reynolds number can also be analyzed through the mean values of the pressure coefficient around the surface of the rotating cylinder. The same Re values of the Fig. 15 are simulated. However, for better visualization, only the pressure distribution for five Re values is plotted. In Fig. (16a), are shown the pressure

https://dx.doi.org/10.22161/ijaers.76.45 *ISSN: 2349-6495(P) | 2456-1908(O)*

distribution along of the upstream cylinder. It can be seen that, at the point of minimum velocity (stagnation point), θ = 0º, the local pressure is maximum and consequently the mean pressure coefficient also, Cp = 1. At the bottom of the cylinder (θ ≈ 90º), it appears that the values for the mean pressure coefficient are higher than those corresponding to the top side, θ ≈ 270º. This is coherent, once a time that, the flow is accelerated at the top and decelerated at the bottom. With the increase of Re up to 3000, a reduction in the pressure coefficient can be seen at the bottom side of the cylinder, and after this Re, an increase is verified, with the mean values being between those obtained for Re 200 and 3000. It is interesting to observe that for Re ≥ 1000 there is an inflection in the curve to the angle approximately equal to 90º. On the other hand, at the top of the cylinder, the coefficient shows variations with the increase in the Re, with the mean values between those obtained for Re 500 and 50000. In addition, it is noted that the curve moves slightly to the right.

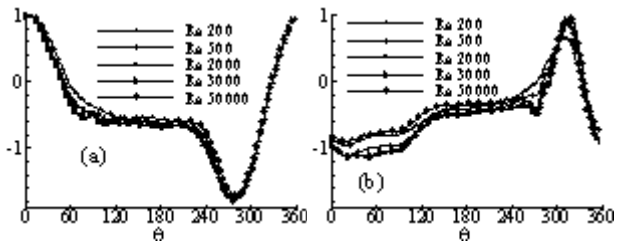

Fig. 16: Mean pressure coefficient in function of the angle

The mean values of the pressure coefficient for the downstream cylinder are shown in Fig. (16b). It can be seen that, at θ = 0º, the local pressure is minimum and consequently the mean pressure coefficient also, Cp ≈ -1.0. This is due to the fact that the shear layers coming from the upper side of the upstream cylinder collide with the front part of the downstream one, reducing the local pressure and consequently the pressure coefficient. Contrary to what is observed for the upstream cylinder, it is noted that the lower side of the cylinder, θ ≈ 90º, has smaller values than the upper side, θ ≈ 270º, for the pressure coefficient. This behavior is coherent, once a time that, the downstream cylinder has a counterclockwise rotation movement. Thus, the flow is accelerated on the lower side (smaller local pressure) and decelerated on the upper side (higher local pressure). It is important to note that the stagnation point, this is, point of minimum velocity and maximum pressure, has changed its position in relation to observed for the upstream one. It is verified a displacement of it towards the top of the cylinder, as shown in Fig. 17, by visualization of the pressure fields, for Reynolds number 2000 and 50000. Here, for Re = 200, it is noted that the maximum mean value of the pressure coefficient, approximately 0.68, is obtained for the angle equal to 310°, less than the maximum value obtained for the upstream cylinder, Cp = 1.0. It is also noted that the Cp presents increasing values, for the angles of approximately 20° up to 310° and then it reduces in an accelerated way until 360°. Along the cylinder, it is verified that there are points at which growth is slower than at others. With the increase of Re to 500, the flow has a similar behavior, however for the angles 20° up to 310°, the mean values showed a reduction and in the range of 300° up to 340° an increase, remaining below 1.0, approximately 0.85. The maximum value of Cp (0.967) is verified for Re = 3000, with the curve moving to the right (from 310° up to 316°, approximately). For the others simulated Re, the mean values are between those obtained for Re = 200 and 3000.

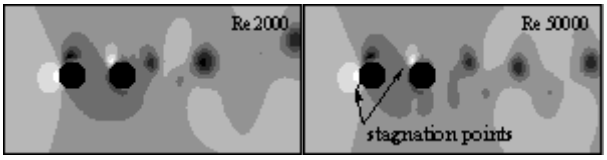

Fig. 17: Pressure fields for L/D = 2.0, α= 0.5.

VI. CONCLUDING REMARKS

Two-dimensional numerical simulations are carried out in order to investigate the flow dynamics around two rotating circular cylinders arranged side by side and in tandem. The results showed that, beside the influence of parameters such as Reynolds number, spacing ratio and specific rotation, on the flow behavior, the arrangement of the cylinders along the flow is also important. This is verified, through the analysis of the vortex shedding mechanism for both cases, considering α = 0.5 and Re = 100. For the side by side case, the suppression of the vortex shedding process is obtained for L/D = 1.5. On the other hand, for the in tandem case, the vortex shedding gradually decreased with the increase in the spacing, and the vortex suppression is obtained for L/D = 3.0 and 3.5 after a dimensionless time of approximately 100. Thus, it is showed the great importance of the cylinder arrangements combined with the spacing ratio on the vortex shedding process, separation of the shear layers and consequently on the wake pattern. It is also verified that, keeping the spacing ratio and Re constant, the flow dynamics is strongly influenced by the specific rotation. In the present work, the critical specific rotation, for which the vortex shedding mechanism is suppressed is 1.3.

It is also found, for the aligned cylinder case, that the Re number has a strong influence on the flow

characteristics, so that the wake seems disorganized, with three-dimensional instabilities and vortices with different sizes and forces. In addition, these characteristics reflect in the drag and lift force, as well as change the fluctuations pattern. Another great influence of cylinder arrangement is relating to the stagnation point of the downstream cylinder that displace towards the top of the cylinder, whereas in the upstream cylinder this point is located at front part, θ= 0°.

Further studies will be performed in order to analyze the flow dynamics around two or more circular cylinders with staggered arrangements and also submitted to others types of movement such as rotational oscillation and one degree of freedom.

ACKNOWLEDGEMENTS

The authors are grateful to the Faculty of Civil Engineering for the support and to the reviewers for their valuable comments and useful recommendations. It is also important to express the acknowledgements to the research grant 306138/2019-0 (A.M.G. de Lima).

REFERENCES

[1] Maliska, C. R. (2004). Heat Transfer and Computational Fluid Mechanics, 2 ed. R.J: LTC, pp. 453.

[2] da Silva, A. R., Silveira-Neto, A., Rade, D. A., Francis, R., Santos, E. A. (2009). Numerical Simulations of Flows over a Pair of Cylinders at Different Arrangements using the Immersed Boundary Method. Computer Modeling in Engineering & Sciences, 50, 3, 285-303.

[3] da Silva, A. R., Silveira-Neto, A., de Lima, A. M. G. (2015). Rotational Oscillation Effect on Flow Characteristics of a Circular Cylinder. World Journal of Mechanics, 5,195-209. http://dx.doi.org/10.4236/wjm.2015.510019

[4] de Lima, A. M. G., da Cunha, B. S. C., da Silva, A. R., Rodovalho, L. F. F. (2017). Vortex-induced vibration analysis of viscoelastically mounted rigid circular cylinders in cross-flow at a moderate Reynolds number. Journal of Vibration and Control, 1-13. doi: 10.1177/1077546317733656

[5] Dienstmann, G., de Almeida, F. S., Fayolle, A., Schnaid, F., Maghous, S. (2018). A simplified approach to transient flow effects induced by rigid cylinder rotation in a porous medium. Computers and Geotechnics, 97, 134-154. https://doi.org/10.1016/j.compgeo.2017.11.014

[6] Xia, Y., Lin, J., Ku, X. (2018). Flow-induced rotation of circular cylinder in Poiseuille flow of Power-law fluids. Journal of Non-Newtonian Fluid Mechanics, 260, 120-132. https://doi.org/10.1016/j.jnnfm.2018.07.003

[7] Wang, X. K., Li, Y. L., Yuan, S. Q., Tan, S. K. (2018). Flow past a near-wall retrograde rotating cylinder at varying rotation and gap ratios. Ocean Engineering, 156, 240-251. https://doi.org/10.1016/j.oceaneng.2018.03.015

[8] Maurya, A., Tiwari, N., Chhabra, R. P. (2019). Effect of a rotating cylinder on the flow of a Bingham plastic fluid in T-junction: Momentum and heat transfer characteristics. International Journal of Heat and Mass Transfer, 143, 118506.https://doi.org/10.1016/j.ijheatmasstransfer.2019.118506

[9] Musmar, S. A., Alrousan, A., Tlili, I. (2019). Effect of cylinder-liner rotation on wear rate: An experimental study. Heliyon, 5, e02065. https://doi.org/10.1016/j.heliyon.2019.e02065

[10] Zou, Q., Ding, L., Wang, H., Wang, J., Zhang, L. (2019). Two-degree-of-freedom flow-induced vibration of a rotating circular cylinder. Ocean Engineering, 191, 106505. https://doi.org/10.1016/j.oceaneng.2019.106505

[11] Bouchon, F., Dubois, T., James, N. (2019). An Immersed Method Based on Cut-Cells for the Simulation of 2D Incompressible Fluid Flows Past Solid Structures. Computer Modeling in Engineering & Sciences, 119, 1, 165-184. CMES. doi:10.32604/cmes.2019.04841

[12] Shu, H., Xu, M., Duan, X., Li, Y., Sun, Y. Li, R., Ding, P. (2020). A Staggered Grid Method for Solving Incompressible Flow on Unstructured Meshes. Computer Modeling in Engineering & Sciences, 123, 2, 509-523. doi:10.32604/cmes.2020.08806

[13] Peskin, C. S. (1977). Numerical Analysis of Blood Flow in the Heart. Journal of Computational Physics, 25, 3, 220-252. https://doi.org/10.1016/0021-9991(77)90100-0

[14] Pan, J-H., Ni, M-J., Zhang, N-M. (2018). A consistent and conservative immersed boundary method for MHD flows and moving boundary problems. Journal of Computational Physics, 373, 425-445. https://doi.org/10.1016/j.jcp.2017.12.034

[15] Fai, T. G., Rycroft, C. H. (2018). Lubricated immersed boundary method in two dimensions. Journal of Computational Physics, 356, 319-339. https://doi.org/10.1016/j.jcp.2017.11.029

[16] Wang, X., Gong, X., Sugiyama, K., Takagi, S., Huang, H. (2020). An immersed boundary method for mass transfer through porous biomembranes under large deformations. Journal of Computational Physics, 413, 109444. https://doi.org/10.1016/j.jcp.2020.109444

[17] Melo, R. R. S., Kinoshita, D., Villar, M. M., Serfaty, R., Neto, A. S. (2020). Numerical experiment of turbulent transfer of thermal energy using the immersed boundary method and adaptive mesh refinement. International Journal of Thermal Sciences, 151,106281. https://doi.org/10.1016/j.ijthermalsci.2020.106281

[18] Li, Z., Dong, B., Tong, F. Wang, W. (2019). An Augmented IB Method & Analysis for Elliptic BVP on Irregular Domains. Computer Modeling in Engineering & Sciences, 119, 1, 63-72. CMES. doi:10.32604/cmes.2019.04635

[19] Majumdar, D., Bose, C., Sarkar, S. (2020). Capturing the dynamical transitions in the flow-field of a flapping foil using Immersed Boundary Method. Journal of Fluids and Structures, 95, 102999. https://doi.org/10.1016/j.jfluidstructs.2020.102999

[20] Lima e Silva, A. L. F., Silva, A. R., Silveira-Neto, A. (2007).

https://dx.doi.org/10.22161/ijaers.76.45 *ISSN: 2349-6495(P) | 2456-1908(O)*

Numerical Simulation of Two-Dimensional Complex Flows around Bluff Bodies using the Immersed Boundary Method. Journal of the Brazilian Society of Mechanical Science and Engineering, 4, 378-386.

[21] Peskin, C. S., McQueen, D. M. (1995). A General Method for the Computer Simulation of Biological Systems Interacting with Fluids. SEB Symp. Soc. Exp. Biol., 49,265-276.

[22] Unverdi, S. O., Tryggvason, G. (1992). A Front-Tracking Method for Viscous, Incompressible, Multi-Fluid Flows. Journal of Computational Physics, 100, 25-37. https://doi.org/10.1016/0021-9991(92)90307-K

[23] Reynolds, O. (1895). On the dynamical theory of incompressible viscous fluids and the determination of the criterion. Philosophical Transactions of the Royal Society of London, 186, Part I, 123-164. https://doi.org/10.1098/rsta.1895.0004

[24] Smagorinsky, J. (1963). General Circulation Experiments with the Primitive Equations. Monthly Weather Review,91, 99-164. https://doi.org/10.1175/1520-0493(1963)091<0099:GCEWTP>2.3.CO;2

[25] Chorin, A. J. (1968). Numerical solution of the Navier-Stokes equations. Math. Comp., 22, 745-762.

[26] Schneider, G. E., Zedan, M. (2007). A Modified Strongly Implicit Procedure for the Numerical Solution of Field Problems. Numerical Heat Transfer, 4,1. https://doi.org/10.1080/01495728108961775

[27] Prasanth, T. K., Behara, S., Singh, S. P., Kumar, R., Mittal, S. (2006). Effect of blockage on vortex-induced vibrations at low Reynolds numbers. Journal of Fluids and Structures, 22, 865-876. doi:10.1016/j.jfluidstructs.2006.04.011

[28] Chen, X-Y., Zha, G-C. (2005). Fully coupled fluid-structural interactions using an efficient high resolution upwind scheme. Journal of Fluid and Structures, 20, 1105-1125. doi:10.1016/j.jfluidstructs.2005.02.011

[29] Yoon, H. S., Chun, H. H., Kim, J. H., Park, I. L. R. (2009). Flow characteristics of two rotating side-by-side circular cylinder. Computer & Fluids, 38, 466-474. doi:10.1016/j.compfluid.2008.0.002

[30] Xiao-hui, G., Jian-zhong, L., Cheng-xu, T., Hao-li, W. (2009). Flow past two rotating circular cylinders in a side-by-side arrangement. Journal of Hydrodynamics, 21, 2, 143-151. doi: 10.1016/S1001-6058(08)60131-6

[31] Zdravkovich, M. M. (2003). Flow around circular cylinders Vol 2: Applications, 2, Oxford Science Publications, ISBN 0-19-856561-5, p.1264.

[32] Hesam, S-M., Navid, N., Behzad, G-D. (2011). Numerical simulation of flow over two side-by-side circular cylinders. Journal of Hydrodynamics, 23, 6, 792-805. doi: 10.1016/S1001-6058(10)60178-3.

[33] Davidson, P. A. (2007). Turbulence An introduction for scientists and engineers, Oxford University Press, ISBN 978-0-19-852949-1, p.657.